*Mon. Not. R. astr. Soc.* (1992) **256,** 111–120

# The role of Compton and Raman scattering in the quasar continuum

R. T. Gangadhara[1,2] and V. Krishan[1]

[1] *Indian Institute of Astrophysics, Bangalore-560 034, India*
[2] *Joint Astronomy Programme, Department of Physics, Indian Institute of Science, Bangalore-560 012, India*

Accepted 1991 November 26. Received 1991 November 18; in original form 1991 April 12

**SUMMARY**

There are three ways in which an electromagnetic wave can undergo scattering in a plasma: (i) when the scattering of radiation occurs by a single electron, it is called Compton Scattering (CS); (ii) if it occurs by a longitudinal electron plasma mode, it is called Stimulated Raman Scattering (SRS), and (iii) if it occurs by a highly damped electron plasma mode, it is called Stimulated Compton Scattering (SCS). The non-thermal continuum of quasars is believed to be produced through the combined action of synchrotron and inverse Compton processes, which are essentially single-particle processes. Here, we investigate the role of SRS and SCS in the generation of continuum radiation from these compact objects. It is shown as an example that the complete spectrum of 3C 273 can be reproduced by suitably combining SCS and SRS. The differential contributions of SCS and SRS under different values of the plasma parameters are also calculated.

## 1 INTRODUCTION

One of the most challenging problems in the area of active galactic nuclei (AGN) is the mechanism of continuum emission. In the broadest sense, the important issues are the mechanisms responsible for the radiation, the kinematics and the spatial distribution of the continuum emitting regions, and the connection of the continuum emission to the central engine. A surprisingly large number of plausible explanations for the origin of this continuum have involved incoherent radiation mechanisms. The most common is synchrotron self-Compton emission from non-thermal electrons, which seems to work rather well from the infrared (IR) to the ultraviolet (UV), particularly for blazars (e.g. Stein & O'Dell 1985; Stein 1988). But the Comptonized, self-absorbed thermal cyclotron radiation from a mildly relativistic electron beam also appears to be able to fit that part of the spectrum (e.g. Begelman 1988). The magnetized accretion disc of a massive black hole acts as an electric dynamo, producing two oppositely directed beams of ultrarelativistic particles (Lovelace 1976). The physics of relativistic jets on submilliarcsecond scales ($\sim 10^{15}$ to $10^{19}$ cm) is discussed by Rees (1984). He has concluded that the power emerges mainly as directed Poynting flux, rather than primarily as particle kinetic energy. The radiative deceleration of ultrarelativistic jets in AGN has been studied by Melia & Königl (1989). The inverse Compton scattering of ambient radiation by a cold relativistic jet in the case of blazars has been studied by Begelman & Sikora (1987).

The collective plasma processes have been shown to play significant roles in the absorption (Krishan 1987; Gangadhara & Krishnan 1990; Beal 1990) and spectral modification of the radiation through its interaction with the plasma in the accretion disc and the emission-line region (Krishan 1988). A sequence of plasma processes, which account for the energy gain and loss of the electron beam, has been discussed by Krishan & Wiita (1986, 1990). In this paper we investigate the scattering of the incident (pump) electromagnetic wave off the electron plasma wave in the two regimes, namely SRS and SCS, and estimate the contribution of these processes in the generation of the complete spectrum from radio to X-rays. The special features, like the threshold of the pump, the growth of the instability, and the angular and spectral distribution of scattered power, are studied under various conditions of electron density and temperature. Using power-law spatial variations of density, Lorentz factor, temperature, and the spectrum of the pump, we reproduce the spectrum of 3C 273. The inclusion of SRS and SCS seems to be essential to account for spectral features of the observed non-thermal spectra of quasars.

## 2 STIMULATED COMPTON AND RAMAN SCATTERING AS ENERGY LOSS MECHANISMS

We begin with the standard model consisting of a black hole of mass $M = 10^8\ M_\odot$ surrounded by relativistic plasma which extends to a few times the Schwarzschild radius $R_s$, ($R_s = 2GM/c^2$) and produces the non-thermal continuum (Wiita 1985). The non-thermal polarized low-frequency electromagnetic wave (soft photon) is considered as a pump

which drives parametric instabilities. This soft photon field may be identified with cyclotron or synchrotron radiation (Stein 1988; Krishan & Wiita 1990). Our model consists of an electron beam which propagates radially outwards and interacts with the soft photon field to produce radiation at higher frequencies. The generation (Blandford & Payne 1982; Wiita, Kapahi & Saikia 1982) and stability of extremely sharp electron beams in the quasar environment has been discussed by Lesch, Schlickeiser & Crusius (1988). The scattering of soft photons off the electron plasma wave, the collective mode of the electrons, can be studied more easily in the rest frame of the electrons, as is done in the study of inverse Compton scattering.

### 2.1 Lorentz transformations

Since it is much simpler to do the non-relativistic calculations in the beam frame, we compute growth rates and the scattered flux in the beam frame and then transfer these quantities to the laboratory frame.

Consider an electron beam moving in the $z$-direction. We use primes on the quantities in the beam frame to distinguish them from the quantities (without primes) in the laboratory frame. The invariance of phase of an electromagnetic wave gives:

$$\boldsymbol{k}_i'\cdot\boldsymbol{r}'-\omega_i't'=\boldsymbol{k}_i\cdot\boldsymbol{r}-\omega_i t. \tag{1}$$

Equation (1) implies that

$$k_x'=k_x, \qquad k_y'=k_y,$$

$$k_z'=\gamma\left(k_z-\frac{v_b}{c^2}\,\omega_i\right), \tag{2}$$

and

$$\omega_i'=\gamma(\omega_i-k_z v_b), \tag{3}$$

where $v_b$ and $\gamma=1/\sqrt{1-v_b^2/c^2}$ are the beam velocity and Lorentz factor, respectively.

The Lorentz transformation of electric field $\boldsymbol{E}$ and magnetic field $\boldsymbol{B}$ to beam frame is given by

$$\boldsymbol{E}_\parallel'=\boldsymbol{E}_\parallel, \qquad \boldsymbol{E}_\perp'=\gamma\left[\boldsymbol{E}_\perp+\frac{\boldsymbol{v}_b}{c}\times\boldsymbol{B}\right], \tag{4}$$

$$\boldsymbol{B}_\parallel'=\boldsymbol{B}_\parallel, \qquad \boldsymbol{B}_\perp'=\gamma\left[\boldsymbol{B}_\perp-\frac{\boldsymbol{v}_b}{c}\times\boldsymbol{E}\right], \tag{5}$$

where the parallel and perpendicular components of $\boldsymbol{E}$ and $\boldsymbol{B}$ are drawn along and perpendicular to $\hat{\boldsymbol{z}}$. Taking $\boldsymbol{E}_\parallel=0$, the angle $\alpha$ between $\boldsymbol{B}_i$ and $\hat{\boldsymbol{z}}$ can be transformed to the beam frame and is given by:

$$\sin(\alpha')=\frac{\sin(\alpha)-v_b/c}{1-(v_b/c)\sin(\alpha)}. \tag{6}$$

The tips of $\boldsymbol{E}'$ and $\boldsymbol{B}'$ lie in a disc of angular width $\approx 2/\gamma$ perpendicular to the beam velocity.

In addition to these quantities, we need the transformation of the plasma frequency, $\omega_p$, the beam thermal speed $v_T$, and the growth rate $\Gamma$.

Since a Lorentz contraction increases both the density and the effective mass by a factor $\gamma$, the plasma frequency $\omega_p$ $(=4\pi n_e e^2/m_e)^{1/2}$ (where $e$ is the electron charge, $n_e$ the beam density and $m_e$ the electron mass) is frame-invariant.

The thermal speed $v_T$ in the beam frame can be expressed in terms of the energy spread of the beam in the laboratory frame as follows. From the definition of $\gamma$, we have

$$v_b=c\left[1-\frac{1}{\gamma^2}\right]^{1/2}. \tag{7}$$

Hence the velocity spread $\delta v_b$ in the laboratory frame is expressed in terms of the spread in $\gamma$,

$$\delta v_b\approx c\,\frac{\Delta\gamma}{\gamma^3}. \tag{8}$$

Now, if we use the Lorentz transformation of velocity $v_z$,

$$\delta v_b=\delta v_z=\frac{\Delta v_z'}{\gamma^2(1+v_b v_z'/c^2)^2}\approx\frac{1}{\gamma^2}\,\Delta v_z'=\frac{v_T}{\gamma^2}, \tag{9}$$

because $v_z'=0$. Hence from equation (9), the thermal speed in the beam frame is obtained:

$$v_T=c\,\frac{\Delta\gamma}{\gamma}. \tag{10}$$

We now consider the transformation of the growth rate $\Gamma$. If a wave with slowly varying amplitude $A'(z', t')$ grows in time and space at a temporal growth rate $\Gamma'$ in the beam frame, then $A'$ satisfies the following equation:

$$\frac{\partial A'}{\partial t'}+v_g'\frac{\partial A'}{\partial z'}=\Gamma' A', \tag{11}$$

where $v_g'$ is the group velocity in the beam frame. Using the Lorentz transformation, we get from equation (11):

$$\frac{\partial A'}{\partial t}+\frac{v_g'+v_b}{1+v_b v_g'/c^2}\,\frac{\partial A'}{\partial z}=\frac{\Gamma}{\gamma(1+v_b v_g'/c^2)}\,A'. \tag{12}$$

The amplitude $A$ in the laboratory frame is linearly proportional to $A'$. Hence the equation (12) gives the Lorentz transformation of the group velocity as well as the growth rate, i.e.,

$$v_g=\frac{v_g'+v_b}{1+v_b v_g'/c^2}\approx\frac{1}{2}\,(v_b+v_g'), \tag{13}$$

$$\Gamma=\frac{\Gamma'}{\gamma(1+v_b v_g'/c^2)}\approx\frac{\Gamma'}{2\gamma}. \tag{14}$$

### 2.2 Stimulated Compton or stimulated Raman scattering?

Consider a large-amplitude plane-polarized electromagnetic pump wave:

$$\boldsymbol{E}_i'=2E_i'\cos(\boldsymbol{k}_i'\cdot\boldsymbol{r}'-\omega_i't')\,\hat{\boldsymbol{x}}', \tag{15}$$

propagating in a homogeneous plasma. In equilibrium, electrons oscillate with velocity $v_i'$ in the pump field $\boldsymbol{E}_i'$. Assume that in a plasma the propagating density perturbation $(\omega', \boldsymbol{k}')$ associated with an electron plasma wave disturbs this equilibrium. The electron density perturbation will grow with the energy of the pump field $\boldsymbol{E}_i'$ and lead to currents at

$\omega' \pm l\omega'_i$, $\boldsymbol{k}' \pm l\boldsymbol{k}'_i$, where $l$ is an integer; the lowest order coupling corresponds to $l=1$. These currents will generate mixed electromagnetic–electrostatic side-band modes at $\omega' \pm l\omega'_i$, $\boldsymbol{k}' \pm l\boldsymbol{k}'_i$. The side-band modes, in turn, interact with the pump wave field, producing a ponderomotive bunching force $\sim \nabla E'^2$ which amplifies the original density perturbation. Thus, there is a positive feedback system which leads to instability, called parametric instability, of the original density perturbation and the side-band modes, provided the rate of transfer of energy into them exceeds their natural damping rates (Drake *et al.* 1974; Liu & Kaw 1976).

For $v'_i/c \ll 1$, it is sufficient to consider only the lowest order coupling ($l=1$) to the side-band modes. We consider a special case of parametric instability in which the high-frequency side-band modes are predominantly electromagnetic, so we essentially have the problem of stimulated scattering where a pump (electromagnetic) wave excites an electron plasma wave ($\omega'_l$, $\boldsymbol{k}'_l$) and two new electromagnetic waves at shifted frequencies: the Stokes mode ($\omega'_s$, $\boldsymbol{k}'_s$) and anti-Stokes mode ($\omega'_{as}$, $\boldsymbol{k}'_{as}$). The instability is excited resonantly only when the following phase matching conditions are satisfied:

$$\omega'_i = \omega'_s + \omega'_l, \tag{16a}$$

$$\boldsymbol{k}'_i = \boldsymbol{k}'_s + \boldsymbol{k}'_l, \tag{16b}$$

$$\omega'_i + \omega'_l = \omega'_{as} \tag{17a}$$

and

$$\boldsymbol{k}'_i + \boldsymbol{k}'_l = \boldsymbol{k}'_{as}. \tag{17b}$$

Each of the excited modes satisfies its own linear dispersion relation in the plasma medium. The dispersion relation of the electron plasma wave in the beam frame is (Hasegawa 1978):

$$1 - \frac{\omega_p^2}{k_l'^2} \int_{-\infty}^{\infty} \frac{\partial f_e/\partial v}{v - (\omega'_l + io)/k'_l}\, dv = 0, \tag{18}$$

where $f_e(v)$ is assumed to be the Maxwellian velocity distribution function of the electrons in the beam frame and $o$ is the small imaginary part of the frequency of the electrostatic perturbation. If we solve equation (17) for $\omega'_l$, we have

$$\omega'_l \approx \omega_p \qquad \text{for } k'_l\lambda'_D \ll 0.4; \tag{19}$$

$$\omega'_l \approx k'_l v_T[1 - io(1)] \qquad \text{for } k'_l\lambda'_D \geq 0.4, \tag{20}$$

where $v_T = [(2/n'_e)\int_{-\infty}^{\infty} v^2 f_e\, dv]^{1/2}$ and $\lambda'_D = (k_B T_e/4\pi n'_e e^2)^{1/2}$ are the thermal speed and Debye length of the electron plasma, respectively ($k_B$ = Boltzman constant). Equation (20) indicates that if $k'_l\lambda'_D$ is greater than or equal to 0.4, then the electron plasma mode loses its wave nature because of its large Landau damping.

The dispersion relation of the electromagnetic wave in a plasma is

$$\omega'^2 = \omega_p^2 + k'^2 c^2. \tag{21}$$

The pump wave, the Stokes mode and the anti-Stokes mode satisfy the dispersion relation (21) in the plasma medium. If the pump wave undergoes backscattering, for $(\omega'_i, \omega'_s) \gg \omega_p$ and $k'_i \approx k'_s$, then $k'_l \approx 2k'_s$. Hence for a given quality of a beam, if $\omega'_s$ is increased by increasing the pump frequency $\omega'_i$, $k'_l$, which may be initially smaller than $0.4/\lambda'_D$, becomes larger than $0.4/\lambda'_D$ at some value of $\omega'_s$. Hence, there exists a critical frequency of the scattered wave above which the scattering process is Compton and below which it becomes Raman. If we write this critical angular frequency in the laboratory frame as $\omega_{cr}$, it can be expressed in terms of beam quality. Using $\omega_{cr} \approx 2\gamma\omega'_s$, $\omega'_s \approx ck'_s$ and $k'_l = 2k'_s = 0.4/\lambda'_D$, we have, with equation (10):

$$\omega_{cr} = 0.4\sqrt{2}\gamma\omega_p \frac{\gamma}{\Delta\gamma}. \tag{22}$$

Thus the critical frequency depends on the relative spread $\Delta\gamma/\gamma$ of the beam energy observed in the laboratory frame, as well as the beam density $n_e$ and $\gamma$.

### 2.3 Growth rates of stimulated Raman and Compton scattering

The most general plasma dispersion relation to describe parametric instability excited in a plasma medium by a large-amplitude coherent electromagnetic wave has been derived by Drake *et al.* (1974) using the Vlasov equation. If the excited side-band modes are predominantly electromagnetic then it reduces to:

$$1 + \frac{1}{\chi'_e(k', \omega')} = k'^2 \left( \frac{|\boldsymbol{k}'_- \times \boldsymbol{v}'_i|^2}{k'^2_- D_-} + \frac{|\boldsymbol{k}'_+ \times \boldsymbol{v}'_i|^2}{k'^2_+ D_+} \right), \tag{23}$$

where $v'_i = eE'_i/m'_e\omega'_i$ is the quiver velocity of electrons, $\omega'_\pm = \omega'_i \pm \omega'$, $\boldsymbol{k}'_\pm = \boldsymbol{k}'_i \pm \boldsymbol{k}'$ and

$$\begin{aligned} D_\pm &= c^2 k'^2_\pm - \omega'^2_\pm + \omega_p^2 \\ &= c^2 k'^2 \pm 2\boldsymbol{k}'\cdot\boldsymbol{k}'_i c^2 \mp 2\omega'\omega'_i - \omega'^2. \end{aligned} \tag{24}$$

In equation (23), when the three-wave interaction is resonant, then $\omega'$ and $\boldsymbol{k}'$ become the angular frequency and wave vector of the electron plasma wave ($\omega'_l$, $\boldsymbol{k}'_l$). The electron susceptibility function is given by (Fried & Conte 1961):

$$\chi'_e(k', \omega') = \frac{1}{(k'\lambda'_D)^2}\left[1 + \frac{\omega'}{k'v_T} Z(\omega'/k'v_T)\right], \tag{25}$$

where

$$Z(\omega'/k'v_T) = \frac{1}{\sqrt{\pi}} \int_{-\infty}^{\infty} \frac{e^{-x^2}}{x - (\omega'/k'v_T)}\, dx, \tag{26}$$

is the plasma dispersion function. The $\chi'_e(k', \omega')$ has the following asymptotic forms:

$$\chi'_e(k', \omega') = \begin{cases} -\dfrac{\omega_p^2}{\omega'^2}\left(1 + \dfrac{3}{2}\dfrac{k'^2 v_T^2}{\omega'^2}\right) + i\dfrac{\sqrt{\pi}}{(k'\lambda'_D)^2} \\ \qquad \times \exp[-\omega'^2/(k'v_T)^2], \quad \text{for } \omega' \gg k'v_T; \\ \dfrac{1}{(k'\lambda'_D)^2}\left(1 + i\sqrt{\pi}\dfrac{\omega'}{k'v_T}\right), \qquad \text{for } \omega' \ll k'v_T. \end{cases} \tag{27}$$

If we use the dispersion relations for $\omega'_i$ (which satisfies equation 21) and $\omega'_l$ (which satisfies 18), the resonant conditions (16a), (16b), (17a) and (17b) can be plotted in a $(\omega, k)$ diagram. In Figs 1 and 2, the arrows show the direction in which energy and momentum transfer from one mode into the other. In the case of backscattering, $[\phi'_s = \cos^{-1}(\hat{\boldsymbol{k}}'_i\cdot\hat{\boldsymbol{k}}'_s) = 180°]$,

$D_- \approx 0$ and $D_+ \neq 0$, therefore, Fig. 1 shows that the Stokes mode is excited but the anti-Stokes mode is not. But in the case of right-angle scattering ($\phi'_s = 90°$) both $D_- \approx 0$ and $D_+ \approx 0$ and hence both the modes are excited as indicated by Fig. 2. The anti-Stokes mode is not excited for $\omega' \ll (c^2 \boldsymbol{k}'_i \cdot \boldsymbol{k}'_l / \omega'_i)$ and it is excited only when the $\boldsymbol{k}'$ is very small or if $\boldsymbol{k}'_l$ is nearly perpendicular to $\boldsymbol{k}'_i$.

When $\omega' \gg k'_l v_T$, the electron plasma mode is well defined and weakly damped. In this case, using $\omega' = \omega'_l + i\Gamma'$ and the asymptotic form of $\chi'_e$, we find from equation (23), with

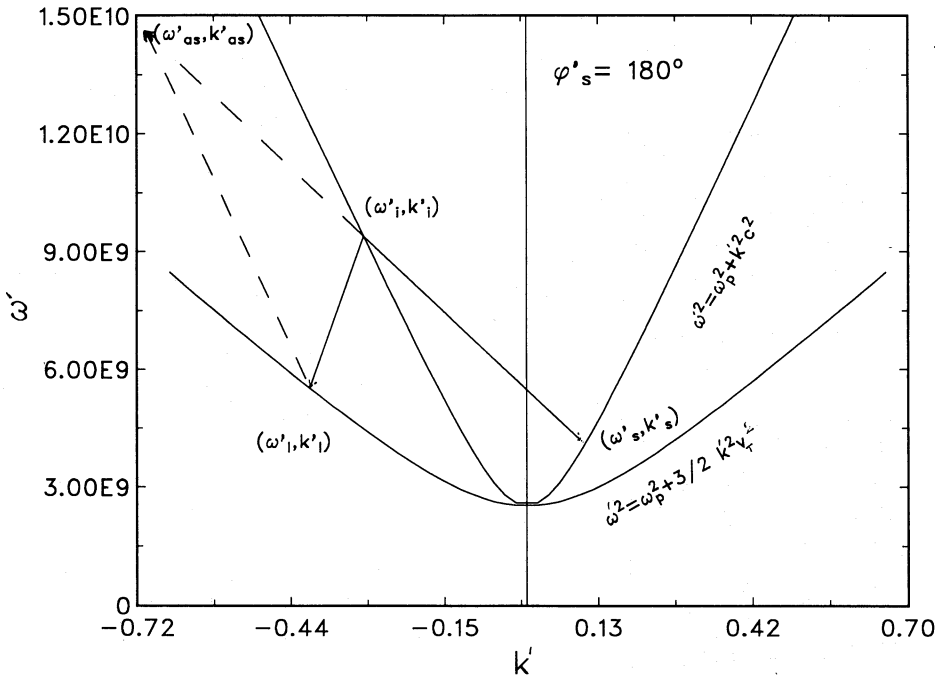


**Figure 1.** Dispersion diagram of the electromagnetic wave and the plasma wave in the beam frame. Arrows on the solid lines indicate the direction of decay of the incident wave ($\omega'_i$, $\boldsymbol{k}'_i$) into Stokes mode ($\omega'_s$, $\boldsymbol{k}'_s$) and electron plasma mode ($\omega'_l$, $\boldsymbol{k}'_l$) during the backscattering of the incident wave. Arrows on the broken lines show the production of the anti-Stokes mode ($\omega'_{as}$, $\boldsymbol{k}'_{as}$). Since ($\omega'_{as}$, $\boldsymbol{k}'_{as}$) does not fall on the dispersion curve of the electromagnetic wave, the anti-Stokes mode is not excited in the backscattering of the incident wave.

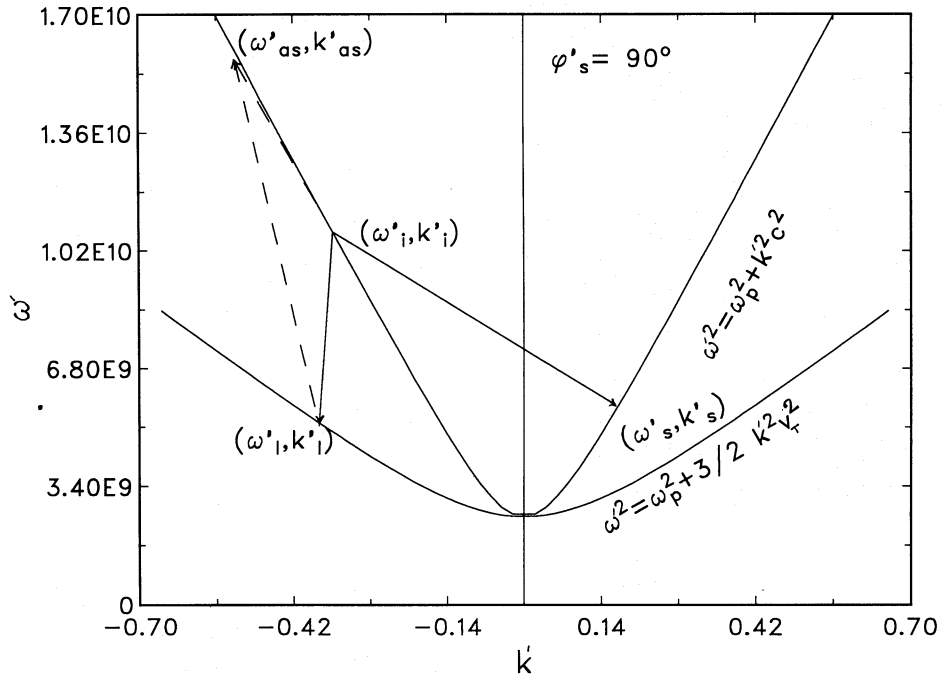


**Figure 2.** Dispersion diagram showing the right-angle scattering of the incident wave ($\omega'_i$, $\boldsymbol{k}'_i$). In this case, both the Stokes mode ($\omega'_s$, $\boldsymbol{k}'_s$) and the anti-Stokes mode ($\omega'_{as}$, $\boldsymbol{k}'_{as}$) are excited. The arrows on the solid lines show the decay of the incident wave into the electron plasma mode ($\omega'_l$, $\boldsymbol{k}'_l$) and the Stokes mode ($\omega'_s$, $\boldsymbol{k}'_s$) and the arrows on the broken lines show the production of the anti-Stokes mode.

$D_+ \neq 0$ (Drake *et al.* 1974):

$$\Gamma'_{SRS} = -\frac{1}{2}(\Gamma'_p + \Gamma'_s) \pm \frac{1}{2}\left[(\Gamma'_p - \Gamma'_s)^2 + 4\frac{v'^2_i}{c^2}\sin^2(\psi'_s)\cos^2(\theta'_e)\,\omega'_i\omega_p\right]^{1/2}. \quad (28)$$

This is the growth rate for stimulated Raman scattering of an electromagnetic wave off a natural electron plasma mode. Here we have introduced $\Gamma'_s = (\omega'_p/\omega'_s)^2\nu'_e/2$ to denote the collisional damping rate of the scattered electromagnetic wave $(\omega'_s, \boldsymbol{k}'_s)$. In equation (28), $\Gamma'_p$ is the damping rate of the electron plasma mode:

$$\Gamma'_p = \frac{\sqrt{\pi}}{2}\frac{\omega_p}{(k'\lambda'_D)^3}\exp\left[-\frac{1}{(k'\lambda'_D)^2} - \frac{3}{2}\right] + \nu'_e.$$

Here we have introduced $\nu'_e = 36.4 n'_e/T_e^{3/2}$ to denote the collisional damping rate of the electron plasma mode, where $T_e$ is the electron temperature. In equation (28), $\theta'_e$ is the angle between $\boldsymbol{k}'_i$ and $\boldsymbol{k}'_l$, and $\psi'_s$ the angle between $\boldsymbol{E}'_i$ and $\boldsymbol{E}'_s$. The growth rate is a maximum when the scattered wave has the same polarization as the incident wave $(\psi'_s = 0)$.

The threshold flux of the pump $S_{thr}$ can readily be obtained by setting $\Gamma'_{SRS} = 0$, in equation (28):

$$S_{thr} = \frac{c^3}{8\pi}\left(\frac{m'_e}{e}\right)^2\frac{\omega'_i}{\omega_p}\frac{\Gamma'_p\Gamma'_-}{\sin(\psi'_s)\cos(\theta'_e)}\ \text{erg cm}^{-2}\,\text{s}^{-1}. \quad (29)$$

We now look for electron plasma modes with frequency $\omega' \approx k'_l v_T$. In this regime, the large argument expansion of electron susceptibility is not valid. Here $k'_l\lambda'_D \geq 0.4$, hence the electron plasma mode in this domain is heavily Landau damped. The growth rate for SCS derived from equation (23) is given by

$$\Gamma'_{SCS} = -2\frac{v'^2_i}{c^2}\sin^2(\psi'_s)\cos^2(\theta'_e)\,\omega'_i\,\text{Im}\left(\frac{\chi'_e}{1+\chi'_e}\right) - \Gamma'_-. \quad (30)$$

The threshold for SCS can be obtained by setting $\Gamma'_{SCS} = 0$.

### 2.4 Numerical solution of equation (23)

When $\omega'_l \approx \omega_p \leq k'_l v_T$ or $k'_l\lambda'_D \approx 0.4$, it is not possible to expand $\chi'_e(\omega', k')$ into an asymptotic series. Therefore, using $\omega' = \omega'_l + i\Gamma'$ we numerically solve equation (23) including all the damping effects. If we separate the real and imaginary parts of equation (23) we get two coupled equations. To find $\omega'_l$ and $\Gamma'$, we solve these two equations with the relation for the plasma dispersion function (equation 26) and its relation with the error function. We have to find the value of $k'_l$ such that it satisfies (16a), (16b), (17a), (17b), (18) and $D_- \approx 0$.

We assume a power-law spatial variation along the path of the beam for electron density $n_e$, Lorentz factor $\gamma$, pump frequency $\nu'_i$ and the pump flux $f_{\nu_i}$, to calculate the growth rate $\Gamma'$ and the scattered flux $f_{\nu_s}$ (calculated in the next section). We find the following power laws give a fairly good agreement with the observed spectrum in the case of 3C 273. The density of the relativistic electron beam follows the power law given by

$$n_e = n_o\left(\frac{r}{r_o}\right)^{-3.2}, \quad (31)$$

where $n_o = 9.24\times10^{17}$ cm$^{-3}$ and $r_o = 10R_s$ for a black hole of mass $M = 10^8\,M_\odot$. In the beam frame, an electron density is given by $n'_e = n_e/\gamma$. The frequency and flux of the soft photon field are assumed to follow the power laws given by:

$$\nu_i = \nu_o\left(\frac{r}{r_o}\right)^{-1.0}, \quad (32)$$

where $\nu_o = 4\times10^{10}$ Hz and

$$f_{\nu_i} = f_o\left(\frac{\nu_i}{\nu_o}\right)^{-0.1}, \quad (33)$$

where $f_o = 7.1\times10^{-25}$ erg cm$^{-2}$ s$^{-1}$ Hz$^{-1}$. Thus we study the scattering of this low-frequency $(\nu_i = \omega_i/2\pi)$ wave with the beam electrons through the processes of SRS and SCS. Here we find that even though $\omega_i < \omega_p$, $\omega'_i > \omega_p$ for $\hat{\boldsymbol{k}}'_i = -\hat{\boldsymbol{z}}'$. Therefore it suffices to take $\omega_i \leq \omega_p$ for $\gamma > 1$ for the present calculations. The radiation field which is isotropic in the laboratory frame becomes beamed in a direction opposite to the beam velocity in the beam frame. In the beam frame, the component of the flux vector of the pump drawn antiparallel $(-\hat{\boldsymbol{z}}')$ to beam velocity becomes much stronger than the perpendicular component. The tips of electric field $\boldsymbol{E}'_i$ and magnetic field $\boldsymbol{B}'_i$ lie in a ring of angular width $\approx 1/\gamma$ perpendicular to the beam velocity. Any anisotropy in the radiation field in the laboratory frame becomes magnified in the beam frame. The power law for the Lorentz factor is assumed to be:

$$\gamma = \gamma_o\left(\frac{r}{r_o}\right)^{-1.2}, \quad (34)$$

where $\gamma_o = 3\times10^3$. We observe that in the beam frame the plasma expands uniformly with the density proportional to $r^{-2}$. The spread in energy of the beam $\Delta\gamma/\gamma$ is assumed to remain constant throughout its path. Also, we assume the scattered radiation has the same polarization as the incident radiation $(\psi'_s = 0)$.

## 3 LIMITING GAIN AND OUTPUT POWER

The scattered radiation fields $\boldsymbol{E}'_s$ and $\boldsymbol{B}'_s$ become large as the instability progresses. At the critical frequency (equation 22) the Lorentz force $\boldsymbol{v}'_i \times \boldsymbol{B}'_s$ begins to act on the electrons. The associated electric potential traps the beam electrons which results in an increase in their thermal spread. The trapping potential $\phi'_t$, due to the Lorentz force $\boldsymbol{v}'_i \times \boldsymbol{B}'_s$ in the beam frame, is obtained from

$$\left|\frac{\partial\phi'_t}{\partial z'}\right| = |k'_l\phi'_t| \approx \frac{1}{c}|v'_i B'^*_s|,$$

given by

$$\phi'_t = \frac{1}{k'_l}\frac{|v'_i|}{c}|B'_s|. \quad (35)$$

The effective thermal speed $v_{T_{eff}}$ due to the trapping potential is

$$v_{T_{eff}} = (2e\phi'_t/m_e)^{1/2}. \quad (36)$$

The growth rate of the instability reaches a maximum ($\Gamma' = \Gamma'_m$) at the critical frequency (equation 22) when $k'_l = \omega_p / v_{T_{eff}}$ (see Fig. 4a) because for $v_{T_{eff}} \geq \omega_p / k'_l$ Landau damping begins to play a dominant role and the gain changes from Raman to Compton. The scattered radiation magnetic field, at the critical frequency, is given by

$$B'_{sm} = \left(\frac{m'_e}{2e}\right) \frac{c}{v'_i} \frac{\omega_p^2}{k'_l}. \tag{37}$$

The growth of the scattered radiation magnetic field $B'_s$ is governed by the equation:

$$\frac{dB'_s}{dt'} = \Gamma' B'_s, \tag{38}$$

where $\Gamma'$ is the growth rate in the beam frame. Integrating (38), we get

$$B'_s(t') = C_1 \exp[\Gamma' t']. \tag{39}$$

The flux vector of the scattered radiation in the beam frame is

$$\boldsymbol{S}' = \frac{c}{4\pi} (\boldsymbol{E}'_s \times \boldsymbol{B}'_s). \tag{40}$$

At $\Gamma' = \Gamma'_m$, $B'_s = B'_{sm}$. We find the flux emitted during the characteristic time $t' = 1/\Gamma'_m$, chosen as the saturation time for instability. Using (39), equation (40) can be written as:

$$S' = \frac{c}{4\pi} B'^2_{sm} \exp\left[2\left(\frac{\Gamma'}{\Gamma'_m} - 1\right)\right]. \tag{41}$$

To transfer flux to the laboratory frame, first we resolve $\boldsymbol{E}'_s$ and $\boldsymbol{B}'_s$ into components $\boldsymbol{E}'_{s_\parallel}$ and $\boldsymbol{B}'_{s_\parallel}$, parallel, and $\boldsymbol{B}'_{s_\perp}$ and $\boldsymbol{E}'_{s_\perp}$, perpendicular to $\hat{\boldsymbol{z}}'$. Now, the flux in the laboratory frame is given by:

$$\boldsymbol{S}_\parallel = \frac{c}{4\pi} \gamma^2 \left[\left(1 + \frac{v_b^2}{c^2}\right) \frac{B'_{s_\perp} E'_{s_\perp}}{v_b} + \frac{E'^2_{s_\perp} + B'^2_{s_\perp}}{c}\right] \boldsymbol{v}_b, \tag{42}$$

$$\boldsymbol{S}_\perp = -\frac{c}{4\pi} \gamma \left[\left(\frac{E'_{s_\perp}}{B'_{s_\perp}} + \frac{v_b}{c}\right) B'_{s_\parallel} \boldsymbol{B}'_{s_\perp} + \left(\frac{B'_{s_\perp}}{E'_{s_\perp}} + \frac{v_b}{c}\right) E'_{s_\parallel} \boldsymbol{E}'_{s_\perp}\right]. \tag{43}$$

Taking $\boldsymbol{E}'_s$, $\boldsymbol{E}'_i$ along $\hat{\boldsymbol{x}}'$, the components of $\boldsymbol{E}'_s$ and $\boldsymbol{B}'_s$ are given by:

$$\begin{aligned} \boldsymbol{B}'_{s_\perp} &= -B'_s \cos(\phi'_s)\, \hat{\boldsymbol{y}}', \qquad \boldsymbol{E}'_{s_\perp} = E'_s \hat{\boldsymbol{x}}', \\ \boldsymbol{B}'_{s_\parallel} &= -B'_s \sin(\phi'_s)\, \hat{\boldsymbol{z}}', \qquad \boldsymbol{E}'_{s_\parallel} = 0, \end{aligned} \tag{44}$$

where $\phi'_s = \cos^{-1}(\hat{\boldsymbol{k}}'_i \cdot \hat{\boldsymbol{k}}'_s)$. Now, the components of the flux vector in the laboratory frame are given by:

$$\boldsymbol{S}_\parallel = \frac{c}{4\pi} \gamma^2 B'^2_{sm} \exp\left[2\left(\frac{\Gamma'}{\Gamma'_m} - 1\right)\right] \times \left\{[1 + \cos^2(\phi'_s)] \frac{v_b}{c} - \left(1 + \frac{v_b^2}{c^2}\right) \cos(\phi'_s)\right\} \hat{\boldsymbol{z}}', \tag{45}$$

$$\boldsymbol{S}_\perp = \frac{c}{4\pi} \gamma B'^2_{sm} \exp\left[2\left(\frac{\Gamma'}{\Gamma'_m} - 1\right)\right] \left[1 - \frac{v_b}{c} \cos(\phi'_s)\right] \sin(\phi'_s)\, \hat{\boldsymbol{y}}'. \tag{46}$$

If the pump field strength is increased it produces a spread in the beam velocity, consequently it decreases the scattered power and increases the growth rate. The component $\boldsymbol{S}_\parallel$ is much stronger than $\boldsymbol{S}_\perp$ because it is proportional to $\gamma^2$, while the latter is proportional to $\gamma$. The scattered radiation gains all its energy from the relativistic electron beam. Consequently, the electron beam gets decelerated due to the interaction with the pump. The emitted radiation is beamed and confined to a cone of angular radius $\approx 1/\gamma$. The scattered radiation flux, at the observer, is given by:

$$f_{\nu_s} = \frac{1}{2} \left(\frac{R_b}{R_e}\right)^2 \frac{S}{\nu_s}, \tag{47}$$

where $S = [S_\parallel^2 + S_\perp^2]^{1/2}$, $\Delta\theta$ is the angular radius of the beam, $R_b = r \tan(\Delta\theta)$ is the radius of the beam at a distance of $r \geq 10 R_s$ from the central engine and $R_e = 7.9 \times 10^8$ pc is the distance between quasar 3C 273 and the Earth. Using the observed value of the flux of 3C 273 at $10^{18}$ Hz, we fix $\Delta\theta = 0.^\circ0065$. We calculate the scattered flux at other frequencies using the spatial variation of plasma parameters as discussed earlier. Thus $R_b$ increases as $r$ increases for constant $\Delta\theta$ at all frequencies.

## 4 DISCUSSION

Figs 1 and 2 show the conditions for SRS and SCS. In Fig. 3, we have plotted $k'_l \lambda'_D$ as a function of the frequency $\nu_i$ of the incident radiation. For the plasma parameters indicated on the figure, we find that in the range $\nu_i \geq \omega_p/\pi$, $k'_l \lambda'_D \leq 0.4$. In this regime, electrons show collective behaviour and the excited electron mode is weakly damped, because its phase velocity is much larger than the thermal velocity of the electrons. Here the scattering of the electromagnetic radiation off the electron plasma mode occurs due to SRS.

For $\nu_i \gg \omega_p/\pi$, we find $k'_l \lambda'_D > 0.4$. Therefore the phase velocity of the electron plasma mode becomes comparable to the thermal velocity of the electrons. This leads to large Landau damping and hence the electrons lose their collective

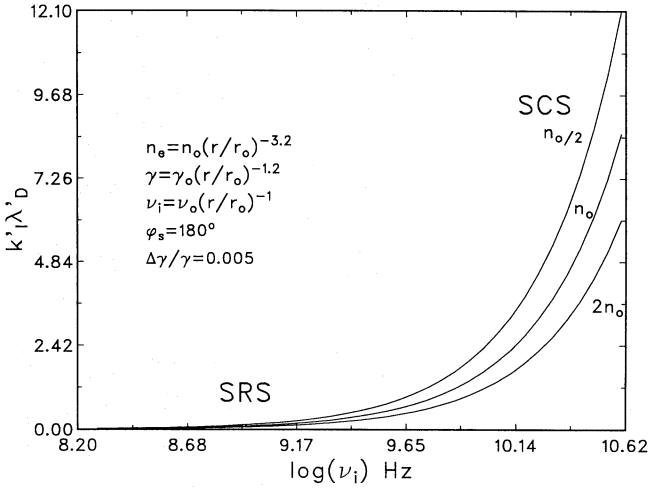


**Figure 3.** The quantity $k'_l \lambda'_D$ versus the frequency of the incident wave $\nu_i$ for three different densities. At $k'_l \lambda'_D \leq 0.4$, SRS occurs and at $k'_l \lambda'_D > 0.4$, SCS occurs. The constants are: $\gamma_o = 3 \times 10^3$, $n_o = 9.24 \times 10^{17}$ cm$^{-3}$, $\nu_o = 4 \times 10^{10}$ Hz.

behaviour. In this case, scattering of the electromagnetic radiation occurs due to a highly damped electron plasma mode and this process is called the SCS process. There are three curves in Fig. 3 for three values of the initial electron density: $n_o$, $n_o/2$ and $2n_o$. At higher density ($2n_o$), since $k_l'\lambda_D'$ approaches 0.4 at higher $\nu_i$ ($=10^{9.65}$ Hz), SRS extends to higher frequencies, while at lower density ($n_o/2$), $k_l'\lambda_D'$ approaches 0.4 at a lower $\nu_i$ ($=10^{9.2}$ Hz), and SRS occurs over a smaller range of incident frequencies.

Fig. 4(a) shows the growth rate as a function of the frequency $\nu_s$ of the backscattered radiation for three different values of initial density: $n_o$, $n_o/2$ and $2n_o$, using the different power laws given on the figure. First consider the curve labelled with $n_o$, in the range $10^{10} \le \nu_s \le 10^{13.85}$ Hz. The growth rate of the backscattering of electromagnetic radiation increases with $\nu_s$ and reaches maximum at $\nu_s = 10^{13.85}$ Hz. As $\nu_s$ is further increased, the electron plasma mode experiences a large Landau damping and in the range $10^{13.85} \le \nu_s \le 10^{14.7}$ Hz, the growth rate decreases rapidly with

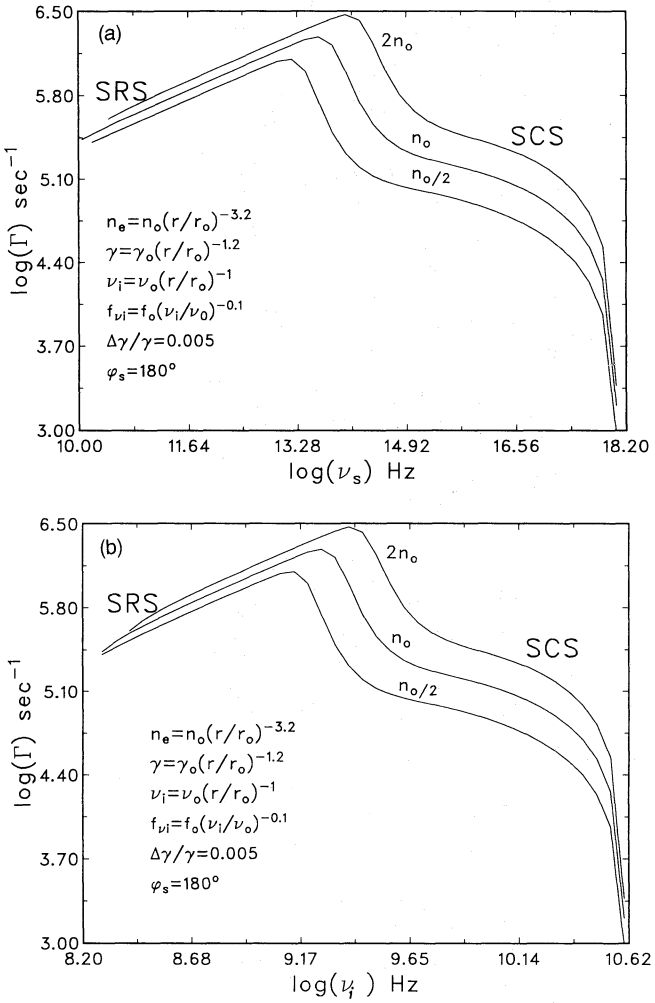


**Figure 4.** (a) Growth rate $\Gamma$ versus scattered wave frequency $\nu_s$ at three different values of electron density in the laboratory frame. At maxima, the scattering process changes from SRS to SCS. The constants are: $\gamma_o = 3\times10^3$, $n_o = 9.24\times10^{17}$ cm$^{-3}$, $\nu_o = 4\times10^{10}$ Hz and $f_o = 7.1\times10^{-25}$ erg cm$^{-2}$ s$^{-1}$ Hz$^{-1}$. (b) Growth rate $\Gamma$ versus incident wave frequency $\nu_i$ at three different values of electron density in the laboratory frame. At maxima, the scattering process changes from SRS to SCS. The constants are as in (a).

$\nu_s$. Further, in the range $10^{14.7} < \nu_s \le 10^{17}$ Hz, due to the saturation of Landau damping, the growth rate shows a slow decrease. For $\nu_s > 10^{17}$ Hz, which occurs rather in the high-density region, the collisional damping rate of the electron plasma mode becomes large, resulting in a sharp decrease in the growth rate. The frequency of the scattered radiation corresponding to maximum growth rate, the critical frequency $\nu_{cr}$, acquires higher values with an increase in density. The scattered radiation of frequency below $\nu_{cr}$ is produced due to the SRS process and above $\nu_{cr}$, due to SCS.

Fig. 4(b) shows the variation of the growth rate as a function of the incident radiation frequency $\nu_i$ for three values of the initial density: $n_o$, $n_o/2$ and $2n_o$. The variation is found to be qualitatively similar to that shown for Fig. 4(a). However, one must note that the bandwidth of the incident radiation is much narrower.

Fig. 5 shows the variation of the growth rate of the backscattered radiation as a function of its frequency $\nu_s$ for three different values of the energy spread $\Delta\gamma/\gamma = 0.0035$, 0.005 and 0.01. First consider the curve labelled with $\Delta\gamma/\gamma = 0.005$. In the range $10^{10} \le \nu_s \le 10^{13.85}$ Hz, the growth rate increases with frequency due to the increase of pump strength and weak damping, and reaches maximum at $\nu_s = 10^{13.85}$ Hz. In the range $10^{13.85} < \nu_s \le 10^{14.7}$ Hz, the electron plasma mode experiences a large Landau damping and hence the growth rate decreases. At still higher frequencies, in the range $10^{14.7} < \nu_s \le 10^{17}$ Hz, the Landau damping reaches saturation, so the growth rate falls slowly. For $\nu_s > 10^{17}$ Hz, due to the large electron density, the collision damping rate becomes large, consequently the growth rate decreases rapidly.

At a lower value of $\Delta\gamma/\gamma$ ($=0.0035$), the Landau damping begins to act at a higher frequency, therefore the growth rate peaks at a higher frequency. On the other hand, if $\Delta\gamma/\gamma$ is large ($=0.01$), then Landau damping begins to act at a lower frequency and hence the growth rate peaks at a lower frequency. Hence the critical frequency $\nu_{cr}$ shifts to a higher frequency when $\Delta\gamma/\gamma$ is small. Since the collision frequency

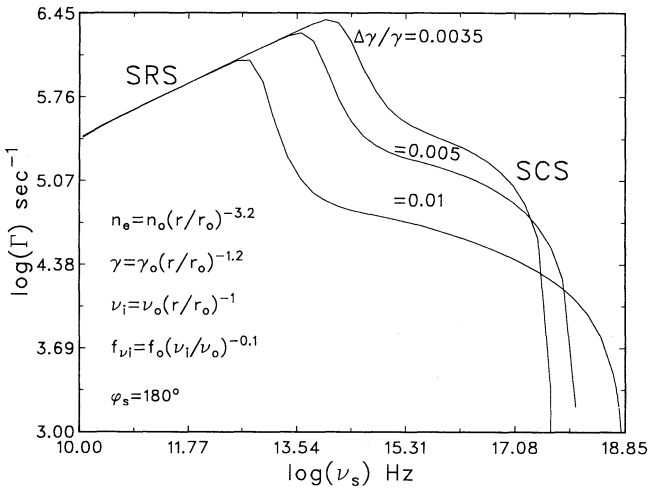


**Figure 5.** Growth rate $\Gamma$ versus scattered wave frequency $\nu_s$ at three different values of $\Delta\gamma/\gamma$. At maxima, the scattering process changes from SRS to SCS. The constants are: $\gamma_o = 3\times10^3$, $n_o = 9.24\times10^{17}$ cm$^{-3}$, $\nu_o = 4\times10^{10}$ Hz and $f_o = 7.1\times10^{-25}$ erg cm$^{-2}$ s$^{-1}$ Hz$^{-1}$.

decreases with increase of $\Delta\gamma/\gamma$, the growth rate becomes non-zero even up to much higher frequencies, i.e., up to $\nu_s > 10^{18}$ Hz. Note that the bandwidth ($10^{8.3} < \nu_i < 10^{10.9}$ Hz) of the incident radiation is much narrower.

Fig. 6 shows the growth rate as a function of scattering angle $\phi_s$ at four different frequencies: $\nu_s = 10^{12}$, $10^{14}$, $10^{16}$ and $10^{17}$ Hz. Here $\phi_s$ is the angle between $\boldsymbol{k}_i$ and $\boldsymbol{k}_s$. The instability is excited in the range $10° < \phi_s' \leq 180°$, but not in the range $0° \leq \phi_s' < 10°$ because in the latter range $k_l'$ becomes imaginary for the plasma parameters given on the figure. Due to the Lorentz transformation of $\phi_s'$ given by

$$\cos(\phi_s) = \frac{\cos(\phi_s') + v_b/c}{1 + (v_b/c)\cos(\phi_s')},$$

$\phi_s$, in the laboratory frame, is confined to a narrow angle about the beam axis. The backscattering, i.e., $\phi_s' = 180°$, corresponds to $\theta_e' = 0$, and the growth rate becomes a maximum, see equation (28). For $\phi_s' < 180°$, $\theta_e'$ increases and hence the growth decreases. At $\nu_s = 10^{14}$ Hz, which is close to the critical frequency, the growth rate peaks at $\phi_s = 179°.2$ and $k_l'\lambda_D'$ approaches 0.4. The growth rate peaks for backscattering at all frequencies except when $\nu_s = 10^{14}$ Hz. The strange behaviour of the growth rate at $\nu_s = 10^{14}$ Hz reflects the transition in the scattering process.

In Fig. 7, the theoretical spectra of the backscattered and incident radiation are plotted (continuous curves). For comparison we have also shown observed points (open circles represent the spectrum of 3C 273, when flare activity was occurring during 1984 February and open triangles represent its normal spectrum observed during 1986 February) from the quasi-simultaneous multifrequency observations of Courvoisier *et al.* (1987). At the critical frequency $\nu_s = 10^{13.85}$ Hz, there is a break in the spectrum due to the change of scattering process from SRS to SCS. The SRS process contributes in the lower frequency part of the spectrum ($\nu_s \leq 10^{13.85}$) while SCS contributes in the higher energy part. The slope of the spectrum in the SRS region is $-0.8$ and in the SCS region it is $-0.7$. The hard X-ray part of the spectrum is steep due to collisional damping and the slope of this part is $-1.5$. The bump in the spectrum is produced at the transition region ($k_l'\lambda_D' = 0.4$) between the SRS and SCS regions.

The dependence of the spectrum on the density of electrons is shown in Fig. 8, where we have chosen three different values for initial density: $n_o$, $2n_o$ and $n_o/2$. The region of higher density and lower scattered frequency corresponds to a weakly damped electron plasma mode and a higher scattered flux $f_{\nu_s}$. The scattered radiation gains its energy from electrons of the relativistic electron beam. Therefore the scattered flux at higher density is greater compared to the flux generated due to the scattering by a damped electron plasma mode at lower density. Note that at higher density, the SRS region extends to even higher frequencies while at

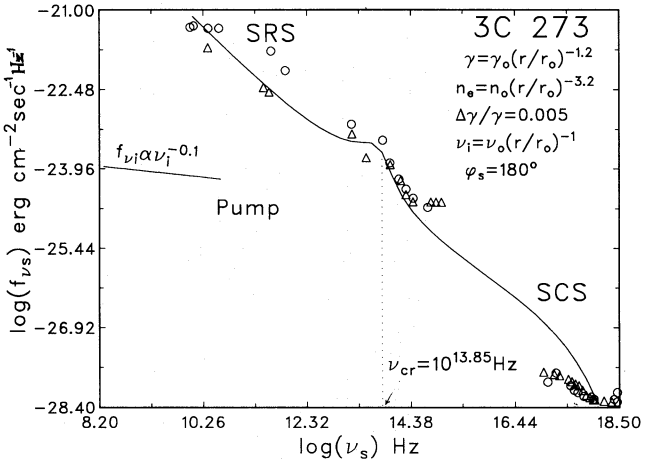


**Figure 7.** The spectrum of the quasar 3C 273. The solid lines represent the calculated spectrum and the spectrum of the pump wave. The observed points, ○ (1984 February) and △ (1986 February) by Courvoisier *et al.* (1987), are also plotted. The constants are: $\gamma_o = 3\times10^3$, $n_o = 9.24\times10^{17}$ cm$^{-3}$, $\nu_o = 4\times10^{10}$ Hz.

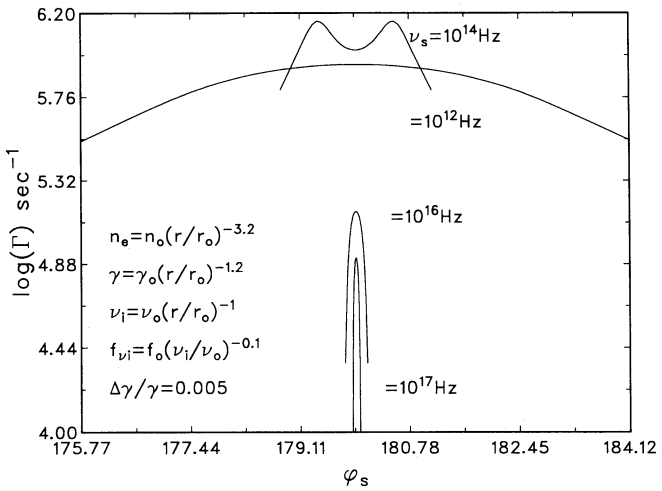


**Figure 6.** The angular dependence of the growth rate $\Gamma$ at four values of scattered radiation frequency $\nu_s$ in the laboratory frame. The angle $\phi_s$ is the angle between $\boldsymbol{k}_i$ and $\boldsymbol{k}_s$. The constants are: $\gamma_o = 3\times10^3$, $n_o = 9.24\times10^{17}$ cm$^{-3}$, $\nu_o = 4\times10^{10}$ Hz and $f_o = 7.1\times10^{-25}$ erg cm$^{-2}$ s$^{-1}$ Hz$^{-1}$.

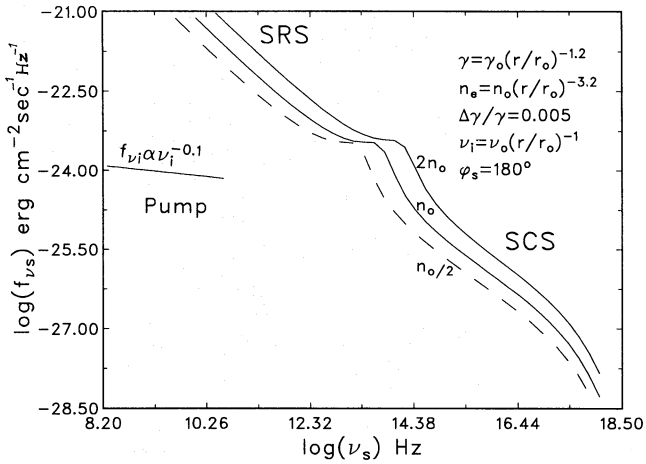


**Figure 8.** The spectrum of the scattered radiation at three different densities: $n_o$, $2n_o$ and $n_o/2$. The SRS occurs at lower frequencies and SCS occurs at higher frequencies. In the transition region between the two there is a bump on each curve which shifts towards higher frequencies with an increase in density. The constants are: $\gamma_o = 3\times10^3$, $n_o = 9.24\times10^{17}$ cm$^{-3}$, $\nu_o = 4\times10^{10}$ Hz.

lower density, SCS extends to lower frequencies. However, the entire spectrum can be produced by either SRS or SCS by choosing the density appropriately, but without any break in the spectrum. Hence the transition region (bump) between SRS and SCS moves to higher frequencies with increasing density.

The effect of change in the energy spread $\Delta\gamma/\gamma$ on the spectrum is shown in Fig. 9 for $\Delta\gamma/\gamma = 0.0035$, 0.005 and 0.01. The bump between the SRS and SCS regions moves towards higher frequencies with the decrease of $\Delta\gamma/\gamma$, because the damping parameter $(k'_l\lambda'_D)$ depends on $\Delta\gamma/\gamma$. Though the scattered flux increases with an increase in $\Delta\gamma/\gamma$, the critical frequency decreases. At a lower value of the energy spread, the entire spectrum can be produced by SRS, whereas at higher values of the energy spread, the entire spectrum can be produced by SCS. Hence the transition region (bump) between SRS and SCS moves to higher frequencies with a decrease in the energy spread.

The dependence of the entire spectrum of the scattered radiation on the scattering angle is shown in Fig. 10 for three different values of the scattering angle: $\phi'_s = 180°$, 120° and 90°. The critical frequency shifts towards lower frequency with decreasing $\phi'_s$. The scattered flux as well as the highest scattered frequency decreases with the decrease of $\phi'_s$; see equations (3), (45) and (46).

Fig. 11 shows the beamed emission of scattered radiation. As the scattering angle $\phi'_s$ is varied from 10° to 180°, the emitted flux in the laboratory frame remains confined to a cone of angular radius $\approx 1/\gamma$ about the beam axis.

Fig. 12 shows the angular distribution of the scattered flux $f_s = \nu_s f_{\nu_s}$. The angular distribution of the scattered flux broadens as the frequency decreases. The flux distribution is higher and narrower at higher frequencies.

## 5 CONCLUSIONS

The conclusions of this paper can be summarized as follows.

(i) Compared to Compton scattering, Raman scattering is a faster process.

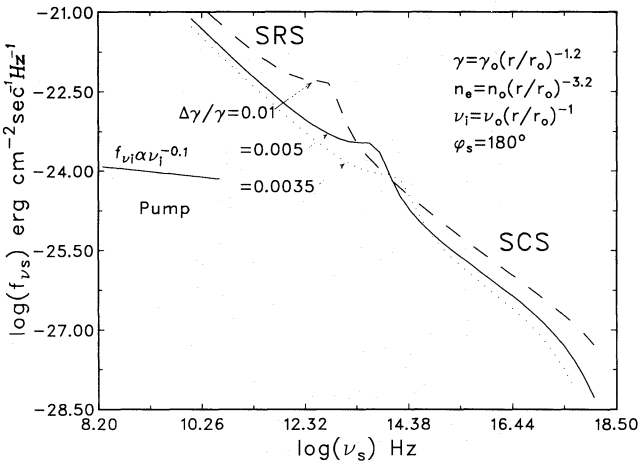


**Figure 9.** The spectrum of the scattered radiation at three different values of $\Delta\gamma/\gamma$. The SRS occurs at lower frequencies and SCS occurs at higher frequencies. In the transition region between the two there is a bump on each curve which shifts towards higher frequencies with a decrease in $\Delta\gamma/\gamma$. The constants are: $\gamma_o = 3\times10^3$, $n_o = 9.24\times10^{17}$ cm$^{-3}$, $\nu_o = 4\times10^{10}$ Hz.

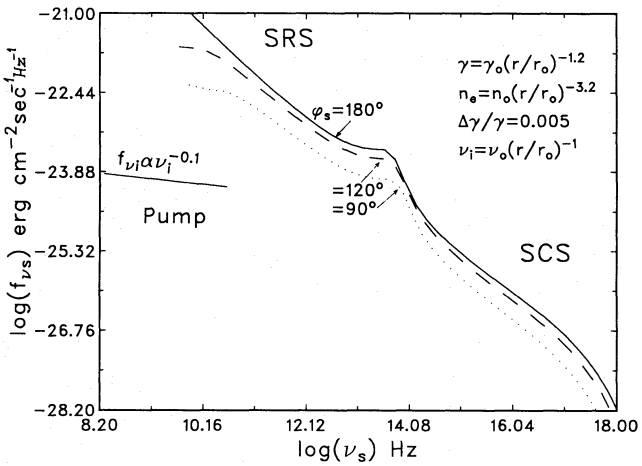


**Figure 10.** The spectrum of the scattered radiation at three values of scattering angle $\phi_s$. The high-frequency end of the spectrum terminates at lower frequency as the scattering angle $\phi_s$ decreases from 180° to 90°. The constants are: $\gamma_o = 3\times10^3$, $n_o = 9.24\times10^{17}$ cm$^{-3}$, $\nu_o = 4\times10^{10}$ Hz.

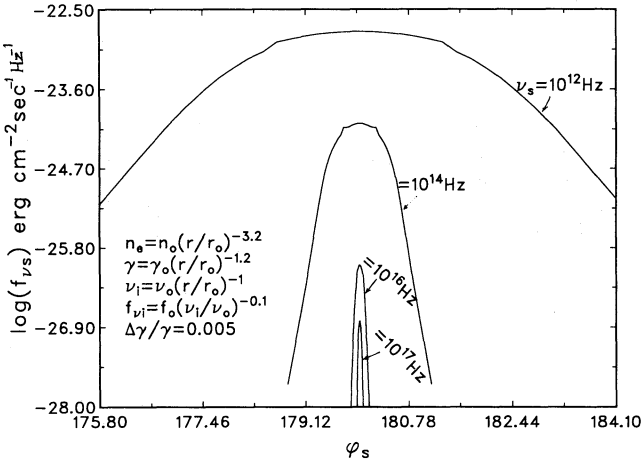


**Figure 11.** The angular distribution of the scattered radiation flux $f_{\nu_s}$ at four scattered radiation frequencies in the laboratory frame. The constants are: $\gamma_o = 3\times10^3$, $n_o = 9.24\times10^{17}$ cm$^{-3}$, $\nu_o = 4\times10^{10}$ Hz and $f_o = 7.1\times10^{-25}$ erg cm$^{-2}$ s$^{-1}$ Hz$^{-1}$.

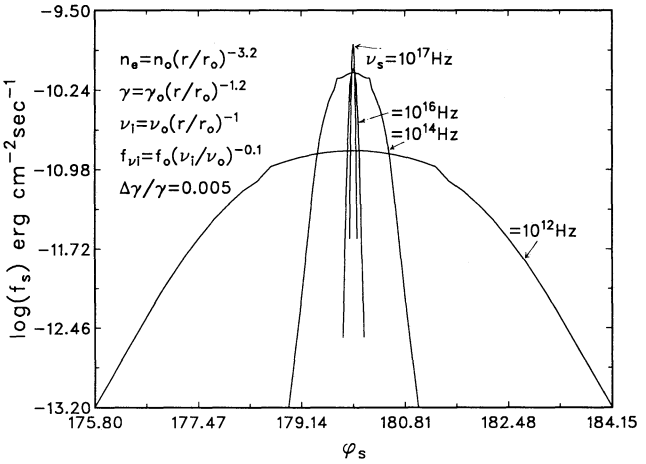


**Figure 12.** The angular distribution of the scattered radiation flux $f_s = \nu_s f_{\nu_s}$ in the laboratory frame. The constants are: $\gamma_o = 3\times10^3$, $n_o = 9.24\times10^{17}$ cm$^{-3}$, $\nu_o = 4\times10^{10}$ Hz and $f_o = 7.1\times10^{-25}$ erg cm$^{-2}$ s$^{-1}$ Hz$^{-1}$.

(ii) At high plasma density $n_e$ and low energy spread $\Delta\gamma/\gamma$, Raman scattering can produce the entire continuum radiation right from radio to X-rays.

(iii) Similarly, at lower density and higher energy spread $\Delta\gamma/\gamma$, Compton scattering can produce the entire continuum radiation right from radio to X-rays.

(iv) For the parameters chosen here, the transition region between SRS and SCS lies where the bump is observed for 3C 273. Thus, we suggest the change of scattering process as one of the possible causes for the spectral break observed in most quasars and AGN.

(v) Raman scattering occurs in a region of density greater than or equal to one quarter of the critical density ($\omega_i' \geq 2\omega_p$).

(vi) An electron beam gets decelerated much faster due to Raman scattering than due to Compton scattering.

(vii) The beamed, stimulated Raman or Compton emission can be detected at a small angle to the electron beam axis. The higher frequency radiation is produced in a narrower angular region around the electron beam axis than the lower frequency radiation.

(viii) As we see, the scattering processes also bring about polarization changes, which we plan to study in detail.

## REFERENCES


Beal, J. H., 1990. In: *Physical Processes in Hot Cosmic Plasmas,* p. 341, eds Brinkmann, W., Fabian, A. C. & Giovannelli, F., Kluwer, Dordrecht.

Begelman, M. C., 1988. In: *Active Galactic Nuclei,* p. 202, eds Miller, H. R. & Wiita, P. J., Springer-Verlag, Heidelberg.

Begelman, M. C. & Sikora, M., 1987. *Astrophys. J.,* **322,** 650.

Blandford, R. D. & Payne, P. G., 1982. *Mon. Not. R. astr. Soc.,* **199,** 883.

Courvoisier, T. J.-L., Turner, M. J. L., Robson, E. I., Gear, W. K., Staubert, R., Blecha, A., Bouchet, P., Falomo, R., Valtonen, M. & Teräsranta, H., 1987. *Astr. Astrophys.,* **176,** 197.

Drake, J. F., Kaw, P. K., Lee, Y. C., Schmidt, G., Liu, C. S. & Rosenbluth, M. N., 1974. *Phys. Fluids,* **17,** 778.

Fried, D. & Conte, S. D., 1961. *The Plasma Dispersion Function,* Academic Press, New York.

Gangadhara, R. T. & Krishan, V., 1990. *J. Astrophys. Astr.,* **11,** 515.

Hasegawa, A., 1978. *Bell System. Tech. J.,* **57,** 3069.

Krishan, V., 1987. *Mon. Not. R. astr. Soc.,* **226,** 629.

Krishan, V., 1988. *Mon. Not. R. astr. Soc.,* **230,** 183.

Krishan, V. & Wiita, P. J., 1986. *Quasars, IAU Symp. No. 199,* p. 419, eds Swarup, G. & Kapahi, V. K., Reidel, Dordrecht.

Krishan, V. & Wiita, P. J., 1990. *Mon. Not. R. astr. Soc.,* **246,** 597.

Lesch, H., Schlickeiser, R. & Crusius, A., 1988. *Astr. Astrophys.,* **200,** L9.

Liu, C. S. & Kaw, P. K., 1976. *Adv. Plasma Phys.,* **6,** 83.

Lovelace, R. V. E., 1976. *Nature,* **262,** 649.

Melia, F. & Königl, A., 1989. *Astrophys. J.,* **340,** 162.

Rees, M. J., 1984. *VLBI and Compact Radio Sources, IAU Symp. No. 110,* p. 207, eds Fanti Kellermann, R. & Setti, G., Reidel, Dordrecht.

Stein, W. A., 1988. In: *Active Galactic Nuclei,* p. 202, eds Miller, H. R. & Wiita, P. J., Springer-Verlag, Heidelberg.

Stein, W. A. & O'Dell, S. L., 1985. In: *Astrophysics of Active Galaxies and Quasi-Stellar Objects,* p. 381, ed. Miller, J. S., University Science Books, Mill Valley.

Wiita, P. J., 1985. *Phys. Repts,* **123,** 117.

Wiita, P. J., Kapahi, V. K. & Saikia, D. J., 1982. *Bull. astr. Soc. India,* **10,** 304.